Black Hole Motion as Catalyst of Orbital Resonances

C. M. Boily[1,†], T. Padmanabhan[2] & A. Paiement[3]

[1] *Observatoire astronomique de l'Université de Strasbourg, CNRS, 11 rue de l'université, F-67000 Strasbourg, France*
[2] *IUCAA, Ganeshkhind Post Bag 4, Pune, India*
[3] *E.N.S.P.S. de Strasbourg, Parc d'innovation, Bd. Sébastien Brant BP 10413, F-67412 Illkirch, France*
[†] *Formerly at: Astronomisches Rechen-Institut, Mönchhofstrasse 12-14 Heidelberg, D-69120 Germany*

2006 December

ABSTRACT

The motion of a black hole about the centre of gravity of its host galaxy induces a strong response from the surrounding stellar population. We treat the case of a harmonic potential analytically and show that half of the stars on circular orbits in that potential shift to an orbit of lower energy, while the other half receive a positive boost and recede to a larger radius. The black hole itself remains on an orbit of fixed amplitude and merely acts as a catalyst of evolution of the stellar energy distribution function $f(E)$. We show that this effect is operative out to a radius of ≈ 3 to 4 times the hole's influence radius, R_{bh}. We use numerical integration to explore more fully the response of a stellar distribution to black hole motion. We consider orbits in a logarithmic potential and compare the response of stars on circular orbits, to the situation of a 'warm' and 'hot' (isotropic) stellar velocity field. While features seen in density maps are now wiped out, the kinematic signature of black hole motion still imprints the stellar line-of-sight mean velocity to a magnitude $\simeq 18\%$ the local root mean-square velocity dispersion σ.

Key words: numerical method: N-body; galaxies, gravitational dynamics

1 Introduction

Black hole dynamics in galactic nuclei has attracted much attention for many years (e.g., Begelman et al. 1984; Kormendy & Richstone 1995; Merritt 2006 for a recent review). The influence of a black hole on its surrounding stars is felt first through the large velocity dispersion and rapid orbital motion of the inner-most cluster stars ($\sigma \sim v_{1d} \lesssim 10^3$ km/s). This sets a scale $\lesssim GM_{bh}/\sigma^2$ ($\simeq 0.015 - 0.019$ pc for the Milky Way, henceforth MW) within which high-angle scattering or stellar stripping and disruption may take place. For the MW, low-impact parameter star-BH encounters are likely given the high density of $\rho \sim 10^7 M_{\odot}/\text{pc}^3$ within a radius of ≈ 10 pc (see e.g. Yu & Tremaine 2003; O'Leary & Loeb 2006; see also Freitag et al. 2006 for a numerical approach to this phenomenon). Star-BH scattering occurring over a relaxation time (Preto et al. 2005 and references therein; Binney & Tremaine 1987) leads to the formation of a Bahcall-Wolf stellar cusp of density $\rho_\star \sim r^{-\gamma}$ where γ falls in the range $3/2$ to $7/4$ (Bahcall & Wolf 1977). Genzel et al. (2003) modeled the kinematics of the inner few parsecs of Sgr A$\star$ with a mass profile $\rho_\star \sim r^{-1.4}$, suggestive of a strong interplay between the black hole and the central stellar cusp. More recently, Schödel et al. (2007) presented a double power-law fit to the data, where the power index $\simeq 1.2$ inside a breaking radius r_{br}, and $\simeq 7/4$ outside, where

$r_{br} \simeq 0.2$ pc. This is indicative of on-going evolution inside r_{br} not accounted for in the Bahcall-Wolf solution.

Most, if not all, studies of galactic nuclei dynamics assume a fixed black hole (or black hole binary) at the centre of coordinates. Genzel et al. (1997) had set a constraint of $\lesssim 10$ km/s for the speed of the black hole relatively to the galactic plane, a constraint later refined to $\lesssim 2$ km/s (Backer & Sramek 1999; Reid & Brunthaler 2004). Stellar dynamics on scales of $\sim$ few pc surrounding Sgr A$\star$ is complex however, and the angular momentum distribution on that scale is a prime example of this complexity (Genzel et al. 2003). Reid et al. (2006) used maser emission maps to compute the mean velocity of 15 SiO emitters relatively to Sgr A$\star$. They compute a mean (three-dimensional) velocity of up to 45 km/s, a result obtained from sampling a volume of $\simeq 1$ pc about the centre[1]. This raises the possibility that stars within the central stellar cusp experience significant streaming motion with respect to Sgr A$\star$. The breaking radius $r_{br} \sim 0.2$ pc is suggestive of uncertain dynamics on that scale. Random, 'Brownian' black hole motion may result from the expected high-deflection angle encounters (Merritt 2005; Merritt et al. 2007). Here we take another

---

[1] Statistical root-n noise $\sim 25\%$ remains large owing to the small number of sources but is inconsequent to the argument being developed here.

approach, and ask what net effect a black hole set on a regular orbit will have on the stars. In doing so, we aim to fill an apparent gap in the modeling of black hole dynamics in dense nuclei, by relaxing further the constraint that the hole be held fixed at the centre of coordinates.

A rough calculation will help to get some orientation into the problem. Consider a point mass falling from rest from a radius R_o in the background potential of the MW stellar cusp. Let the radial mass profile of the cusp $\rho_\star(r) \propto r^{-3/2}$, consistent with MW kinematic data. If we define the black hole radius of influence $\simeq 1$ pc to be the radius where the integrated mass $M_\star(< r) =$ the black hole mass $\simeq 3$ to $4 \times 10^6 M_\odot$ (Genzel et al. 2003; Ghez et al. 2005), then R_o may be expressed in terms of the maximum black hole speed in the MW potential as

$$\left[\frac{\max\{v\}}{100\,\mathrm{km/s}} \right]^{\frac{4}{5}} = \frac{R_o}{1\,\mathrm{pc}}\,.$$

For a maximum velocity in the range 10 to 40 km/s we find $R_o \simeq 0.3 - 0.5$ pc, or the same fraction of its radius of influence[2]. We ask what impact this motion might have on the surrounding stars. To proceed further, let us focus on a circular stellar orbit outside R_o in the combined potential of the black hole and an axisymmetric galaxy. Fig. 1 gives a clue to the analysis. When the black hole is at rest at the centre of coordinates, the star continues on a closed circular orbit of radius r and constant velocity v. We now set the black hole on a radial path of amplitude R_o down the horizontal x-axis. Without loss of generality, let the angular frequency of the stellar orbit be ω', and that of the black hole $\omega \geqslant \omega'$. The ratio $\omega/\omega' \geqslant 1$ is otherwise unbounded. The net force $\boldsymbol{F}$ acting on the star can always be expressed as the sum of a radial component $\boldsymbol{F}_r$ and a force parallel to the x-axis which we take to be of the form $F_x \cos(\omega t + \varphi)$; clearly the constant $F_x = 0$ when $R_o = 0$. The net mechanical work done on the star by the black hole as the star completes one orbit is computed from the integral

$$\delta W = \int \boldsymbol{F} \cdot \boldsymbol{v}\,\mathrm{d}t = \int F_x v \sin(\omega' t) \cos(\omega t + \varphi)\,\mathrm{d}t \qquad (1)$$

where φ is the relative phase between the stellar and black hole orbits. The result of integrating (1) is best set in terms of the variable $\nu \equiv \omega/\omega'$ as

$$\frac{\delta W}{r F_x} = \frac{1}{\nu^2 - 1} \left[\cos(2\pi\nu + \varphi) - \cos(\varphi) \right] \qquad (2)$$

when $\nu > 1$, and

$$\frac{\delta W}{r F_x} = \pi \sin(\varphi) \qquad (3)$$

when $\nu = 1$. It is a simple exercise to show that this last expression is recovered from (2) in the limit $\nu \to 1^+$. Equation (3) embodies the essential feature, which is that δW

Figure 1. Cartoon representing a star on a circular orbit in the combined potential of a black hole and a background galaxy. The black hole motion of amplitude R_o runs parallel to the horizontal x-axis. The net force $\boldsymbol{F}$ acting on the star may be decomposed in a radial component $\boldsymbol{F}_r$ and an x-component.

changes sign when the phase φ shifts to $\varphi + \pi$. Thus whenever the stellar phase-space density is well sampled and all values of $\varphi : [0, 2\pi]$ are realised with equal probability, half the stars receive mechanical energy ($\delta W > 0$) and half give off energy ($\delta W < 0$). In other words, stars in the first quadrant will exchange energy with those in the third quadrant of a Cartesian coordinate system. (Similarly for those in the second and fourth quadrants.) By construction, the black hole neither receives nor loses energy but merely acts as a *catalyst* for the redistribution of mechanical energy between the stars. Our goal, then, is to explore the consequences of this mechanism quantitatively for realistic stellar distribution functions.

We begin with an analysis of star-BH orbit coupling in a harmonic (uniform density) galactic potential (§2). While this choice may appear artificial and an over-simplification, it circumscribes all latitude allowed by uncertainties in the spatial distribution of stars within the black hole influence radius. Furthermore, the basic mechanics is more tractable for that case. This is then extended to the case of a logarithmic potential (§§3 and 4). To cover a wider range of parameters, we explore with a response code the evolution of individual orbits in the time-dependent potential. We show that black hole motion shapes up the energy distribution function, as well as the line-of-sight velocity, which we measure as rms deviations from expected values. The magnitude of these deviations rise monotonically with the amplitude of the black hole's orbit, and its mass. Finally, in §5 we discuss some applications and explore possible extensions to our analysis.

---

[2] These figures are robust to details of the stellar cusp mass profile, so for instance a flat density profile ($\gamma = 0$) would yield R_o in the range 0.3 to 0.6 pc.

2 Circular orbits in a harmonic potential

We start with the case of a star initially on a circular path in a background harmonic potential. The star's orbit for that problem is obtained by solving the equations of a decoupled oscillator; these read in Cartesian coordinates

$$\ddot{\boldsymbol{x}} = -\omega^2 \boldsymbol{x} \tag{4}$$

where

$$\omega \equiv \sqrt{4\pi\, G\rho/3}$$

is the harmonic angular frequency in an axially-symmetric galaxy of uniform density ρ. Adding a fixed black hole of mass M_{bh} at the centre of the coordinates preserves the symmetry of the force-field: the motion may still be described by (4) but with a different angular frequency $\omega' > \omega$. Each circular orbit of the harmonic potential maps to a circular orbit in this new potential. The aim, then, is to find out what happens once the black hole is set in motion, so breaking the symmetry of the force field.

2.1 Co-planar, radial BH motion

We consider a two-dimensional system so all orbits are coplanar. Let the position of the black hole be denoted R and we take $M_{bh} \gg m_\star$. The black hole obeys the same equations (4) for any value of R not exceeding the uniform-density core of the model potential. (A Bahcall-Wolf cusp would soon develop around the centre once the black hole has settled there; the harmonic potential would remain largely unperturbed until that happens.) We define the black hole radius of influence R_{bh} such that

$$M_{bh} \equiv 4\pi\rho R_{bh}^3/3 \tag{5}$$

which we will use again later in a study of the logarithmic potential. As a first important case study we set the black hole on a purely radial path down the x-axis: $\boldsymbol{R} = R\hat{\boldsymbol{x}}$ (from here onwards a hat denotes a unit vector). Equation (2) gives an expression for the mechanical work for the case of a one-dimensional force component. We here develop a second approach based on a limited series expansion of the potential. The full potential

$$\Phi(r,t) = \frac{\omega^2}{2}r^2 - \frac{GM_{bh}}{\sqrt{(x-R[t])^2 + y^2}}$$

simplifies to

$$\Phi(r,t) = \frac{\omega^2}{2}r^2 - \frac{GM_{bh}}{r}\left(1 - \frac{1}{2}\frac{R^2 - 2xR}{r^2} + O([R/r]^3)\right) \tag{6}$$

when we take $r > R$ and truncate a Taylor expansion to leave out all terms of order higher than quadrupolar. In this limit the force acting on the star is easily obtained by differencing (6) with respect to $\boldsymbol{r}$. A closed integral through one revolution on the circular stellar path $\boldsymbol{l}$ yields the net work done on the star by the time-dependent potential:

$$W = -\int \boldsymbol{\nabla}\Phi \mathrm{d}\boldsymbol{l} = \int_0^{2\pi} \boldsymbol{\nabla}\Phi\, r\mathrm{d}\theta\, \hat{\boldsymbol{\theta}} \ . \tag{7}$$

The only non-vanishing contribution to the integral comes from the non-axially symmetric term of the force field; we find:

$$W = -\int_0^{2\pi} \frac{GM_{bh}}{r^2}\frac{R}{r}r\mathrm{d}\theta\,(\hat{\boldsymbol{x}}\cdot\hat{\boldsymbol{\theta}}) = \int_0^{2\pi} \frac{GM_{bh}}{r^2}\frac{R}{r}\sin\theta\, r\mathrm{d}\theta \ . \tag{8}$$

For circular motion, we may always write $r\mathrm{d}\theta = v_c\mathrm{d}t$ with both circular velocity v_c and radius r held constant. The ratio $v_c/(\omega r)$ satisfies

$$\left(\frac{v_c}{r\omega}\right)^2 = 1 + \frac{GM_{bh}}{\omega^2 r^3} = 1 + \frac{M_{bh}}{M_g(<r)} \equiv \mathcal{M} \tag{9}$$

where $\mathcal{M} \in [1, \infty[$ and M_g is the integrated galactic mass inside the orbit *of the star*. We have $\mathcal{M} = 2$ when $r = R_{bh}$ by definition, and $\lim_{r\to\infty} \mathcal{M} = 1$. To progress further requires a specific form for $R(t)$. Solving (4) for a radial orbit down the x-axis we find

$$\boldsymbol{R}(t) = R_o \sin(\omega t + \phi_o)\hat{x} \tag{10}$$

where R_o, ϕ_o are the amplitude and phase of the black hole orbit. The initial conditions are completely specified if we pick the phase of the stellar orbit such that the azimuthal angle $\theta = 0$ when $t = 0$. On integrating (8), we obtain

$$W = -\frac{R_o}{r}\frac{GM_g(<r)\mathcal{M}}{r}\left(\sin[\frac{2\pi}{\sqrt{\mathcal{M}}} + \phi_o] - \sin[\phi_o]\right) \ . \tag{11}$$

Written in this way we recover a direct proportionality between W and the amplitude R_o (and hence $W = 0$ for zero motion, as expected). W assumes both positive and negative values according to the phase ϕ_o. There can be no correlation between ϕ_o and the star's orbit, and hence at a given radius r (or, equivalently, binding energy E) as many stars receive a positive energy increase as those that receive a negative contribution. This impoverishes the occupation level at r (or, E) and creates a hollow feature in the stellar distribution function.

The work W is a periodic function of $\phi_o : [0, 2\pi]$. In this interval, W vanishes whenever any of the following conditions is met:

$$\mathcal{M} = \begin{cases} \left(\dfrac{2\pi}{\pi - 2\phi_o}\right)^2, & \phi_o < \dfrac{\pi}{2} \ , \\[2ex] \left(\dfrac{2\pi}{3\pi - 2\phi_o}\right)^2, & \dfrac{\pi}{2} \leqslant \phi_o \leqslant \dfrac{3\pi}{2} \\[2ex] \left(\dfrac{2\pi}{5\pi - 2\phi_o}\right)^2, & \phi_o > \dfrac{3\pi}{2} \ . \end{cases} \tag{12}$$

The full range of values of $\mathcal{M}$ are covered in the quadrants $-\pi/2 < \phi_o < \pi/2$ and $\pi/2 < \phi_o < 3\pi/2$. As a function of ϕ_o we find as many points outside as inside the radius of influence $\mathcal{M} = 2$ (Fig. 2). For an orbital configuration such that $R_o < r \ll R_{bh}$ a large ensemble of solutions to (12) will cover a wide range of values of $\mathcal{M} > 2$. This will be the case
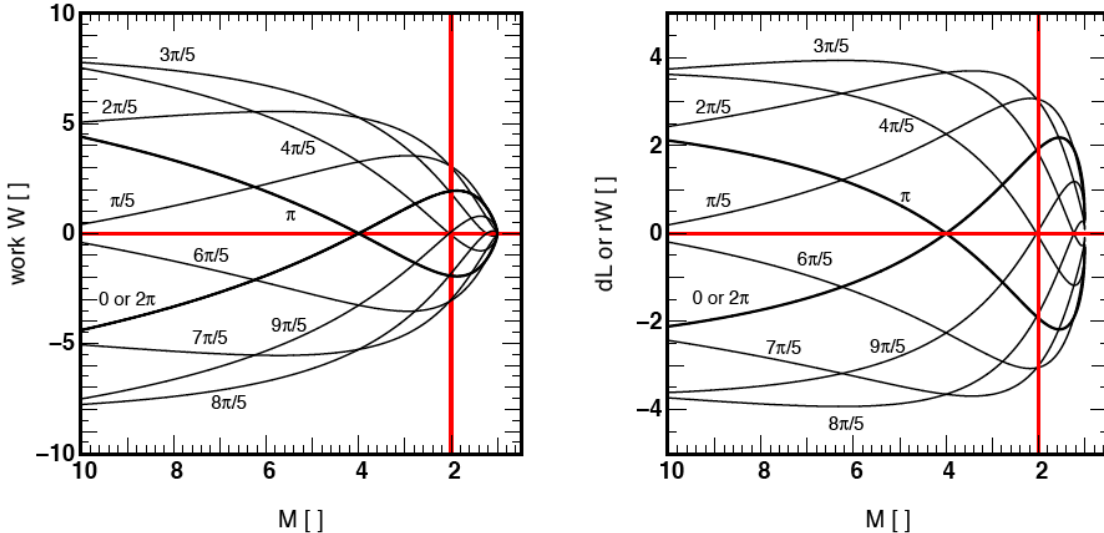
Figure 2. Left-hand panel: the net work W as function of the dimensionless parameter $\mathcal{M}$ defined in (9). Note that W has been renormalised for better clarity. Right-hand panel: the angular momentum dL accrued during one revolution as function of $\mathcal{M}$. The curves are labeled with the phase angle ϕ_o. Note that the radius r would increase from left to right on the figure. The vertical straight line at $\mathcal{M} = 2$ corresponds to $r = R_{bh}$, while $\mathcal{M} = 1$ when $r \to \infty$.

during the final stages of a black hole settling at the heart of a galaxy since then $R_o \to 0$. It is interesting to investigate whether configurations satisfying (12) yield islands of stability or attractors in phase space. Fig. 2 shows the net work done on a circular stellar orbit by the black hole as function of $\mathcal{M}$ for different values of ϕ_o. To determine whether an orbit will be trapped around a point for which $W = 0$, it is sufficient to look at the sign of W in relation to $\mathcal{M}$. Orbits with $\mathcal{M} < 2$ lie outside the influence radius R_{bh} at large distances. A gain in binding energy would shift the orbit to smaller radii requiring $W < 0$. Similarly, an orbit for which $\mathcal{M} \gg 1$ would shift to higher energy whenever $W > 0$, and so move outwards to larger distance (decreasing M). Thus curves of W for which $dW/d\mathcal{M} > 0$ when $W = 0$ would trap orbits, otherwise not. We note that the migration induced through W impacts directly on the angular momentum of the star. This is most clearly seen from the torque $\boldsymbol{\Gamma} = d\boldsymbol{L}/dt = \boldsymbol{\nabla}\Phi \times \boldsymbol{r} = -GM_{bh}/r^3 R(t) \sin\theta \hat{z}$. On integrating over one (stellar) revolution it is easy to show that $|d\boldsymbol{L}| \propto rW$. At a given radius, the sign of $d\boldsymbol{L}$ is a function of ϕ_o alone (see Fig.2[b]). For a well-mixed systems, half the stars will gain angular momentum and move outwards. Since the background galactic potential is taken to be axially symmetric, the distribution of angular momentum at r can then be traced back directly to the quality of the black hole orbit (i.e., its amplitude and frequency).

It is interesting to map out the minimum and maximum values of W achieved as a function of ϕ_o. An extremum of W occurs when the angle ϕ_o satisfies $\cos(2\pi/\sqrt{\mathcal{M}} + \phi_o) = \cos(\phi_o)$ for any constant $\mathcal{M}$ (or equivalently, r). Fig. 3 graphs the results as a function of the phase angle ϕ_o. The results were obtained by setting a range of $\mathcal{M} : [1, 100]$ for

the mass variable. Recall that $\mathcal{M} \to \infty$ as $r \to 0$. The two curves on Fig. 3 coincide if we perform a reflection through $W = 0$ together with a shift of ϕ_o by π radians (180°). The figure shows that when a (positive) maximum is large, the corresponding (negative) minimum is small, and *vice-versa*. It follows that for a finite interval of the phase angle ϕ_o, for instance, all stars which fall in that interval may suffer a net positive (or, negative) intake of energy, irrespective of their orbital radius. Therefore for adequate initial conditions, the energy input from the black hole may leave a signature in the distribution function of the stars robust against any bias that might be attributed to domain decomposition (sampling by radius, energy, etc). By contrast, stars for which $\max(W) \approx |\min(W)|$ would suffer essentially no effect from the black hole. Initial conditions such that $\phi_o \approx \pi/3$ radians ($\approx 52.7^o$) or $\phi_o \approx 4\pi/3$ (233°) are possible examples (cf. Fig. 3).

By virtue of (9) and (11), we find in the limit of large $\mathcal{M}$ that the work $W \propto M^{1/6} \to \infty$. Hence W diverges as $r \to 0$. This should not come as a surprise since in that limit the orbit is Keplerian around the moving black hole, and hence it can not remain close to circular about the centre of co-ordinates, as we have implied so far. Our development will therefore break down when the potential is dominated by the central point source. With M = 100, the largest value considered here, the model galaxy contributes 1% of the dynamical mass only. For the MW galaxy, this would translate to a radius around Sgr A⋆ of ≈ 0.05 pc (Genzel et al. 2003). Stellar collisions are predicted to be important on a scale of 0.1 pc (Yu & Tremaine 2003; O'Leary & Loeb 2006; Merritt 2006). Therefore, if Milky Way data serve as a test case, we should always set $\mathcal{M} \ll 100$.
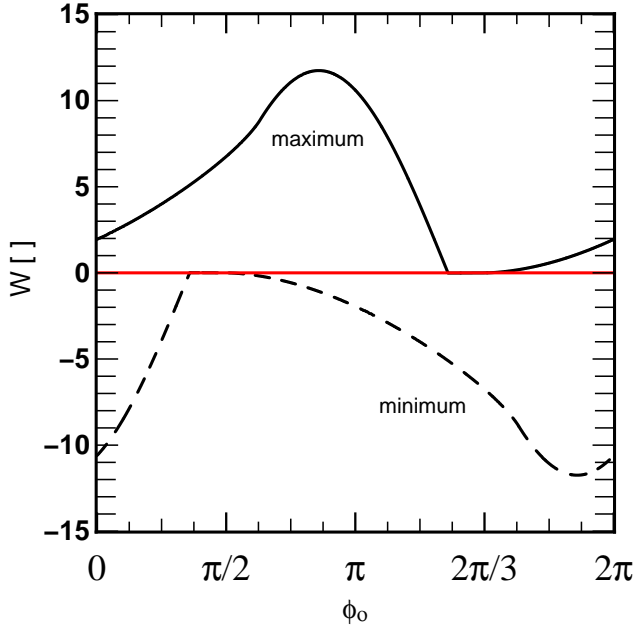
Figure 3. This graphs the maximum (solid) and minimum (dash) value of the work W as a function of the phase angle ϕ_o (in radians). The two curves coincide when reflected through $W = 0$ and shifted by $\delta\phi_o = \pi$ rad.

A final comment concerning the regime $\mathcal{M} \gg 1$. The definition (9) is the ratio of the star's angular frequency to the galactic angular frequency ω. Thus whenever $\mathcal{M} \gg 1$, the star revolves rapidly around the black hole. Such trapped orbits remain circular to a good approximation when viewed in the reference frame of the black hole. (The eccentricity $e = 0$ is an adiabatic invariant.) Orbit trapping and resonant relaxation of non-circular Keplerian orbits have been discussed by various authors (e.g., Tremaine 1995; Rauch & Tremaine 1996; Zhao, Haehnelt & Rees 2002; Merritt 2006).

2.2 Circular black hole motion

2.2.1 Single black hole

It is straightforward to extend the case of radial black hole motion to one where the black hole is on a circular orbit. The results of §2.1 are independent of the sense of rotation of the stellar orbit. The non-zero black hole angular momentum $\boldsymbol{L}_{bh} = \boldsymbol{R} \times \boldsymbol{p}$ breaks this invariance. The work W will differ when stellar and black hole momenta are aligned ($\boldsymbol{L}_{bh} \cdot \boldsymbol{L}_\star > 0$) or anti-aligned ($\boldsymbol{L}_{bh} \cdot \boldsymbol{L}_\star < 0$), a shown by e.g. Toomre & Toomre (1972) in their classic study of interacting spiral galaxies.

Consider a black hole on a clockwise two-dimensional circular orbit of radius R_o,

$$\boldsymbol{R}(t) = R_o \left(\sin(\omega t + \phi_o)\,\hat{\boldsymbol{x}} + cos(\omega t + \phi_o)\,\hat{\boldsymbol{y}} \right) \quad (13)$$

in a self-evident extension to (10). Repeating the same steps that led to (6) will give an extra term for the y-component in the potential which is otherwise identical. When computing the work (7) we may now distinguish between anti- and

clockwise stellar orbits with the notation $d\theta = \pm v_c/r\, dt$. The integration yields

$$W = -\frac{R_o}{r}\frac{GM_g\mathcal{M}}{r}(1 \mp 1)\left(\sin[\frac{2\pi}{\sqrt{\mathcal{M}}} + \phi_o] - \sin[\phi_o] \right). \quad (14)$$

This equation shows that aligned orbits double their energy intake from the black hole, while anti-aligned ones see a net cancellation. The black hole would, therefore, introduce anisotropy in an initially isotropic stellar velocity distribution function. This is not unlike the bar amplification process proposed by Lynden-Bell (1979): the angular frequency ω set the rotation speed of a constant-magnitude quadrupole, as in a barred galaxy. However here the perturbation to the axisymmetric galactic potential is not the two-fold symmetric $m = 2$ mode, but the $m = 0$ lopsided mode.

2.2.2 Binary black hole

The case of a binary black hole of constant separation and centered at the origin of coordinates is derived from (14) through a thought experiment. We imagine that the binding energy of the binary is large and so neglect the background galactic potential. We consider the total contribution of the binary to W as a sum of two single BH's on circular orbits. The phase ϕ_o of one black hole (say, the secondary) is shifted by π radians with respect to that of the primary. On inspection of (14) it follows that whenever the product $R_o\mathcal{M}$ is the same for each BH, the total work W must vanish for any phase angle ϕ_o. This will be the case only when the binary as components of equal mass. Since there is no reason to presume identical masses in general, we would find

$$W = -\frac{R_{o,2} - R_{o,1}}{r}\frac{GM_g}{r}(1 \mp 1)\left(\sin[\frac{2\pi}{\sqrt{\mathcal{M}}} + \phi_o] - \sin[\phi_o] \right)$$

where we have used $R_{o,1} = R_{o,2}\, M_{bh,2}/M_{bh,1}$. The limit where $M_{bh,2} \ll M_{bh,1}$ reduces to the case of a single BH (the secondary) in orbit in the axi-symmetric potential of the primary at rest at the origin of coordinates. Such a situation might occur when a swarm of intermediate mass black holes revolve around a massive hole, presumably the result of repeated coalescence. O'Leary & Loeb (2006) have recently explored the scattering of stars in such a cluster of massive objects.

3 Case study: the logarithmic potential

The coupling between black hole motion and orbits in the harmonic potential is indicative of trends that may develop in more realistic potentials. Here we recast our problem in the framework of the logarithmic potential, which we write as

$$\Phi_g(\boldsymbol{r}) = -\tfrac{1}{2}v_o^2 \ln \left| \frac{x^2 + y^2/q^2 + R_c^2}{R_c^2} \right| \quad (15)$$

with v_o the constant circular velocity at large distances, and $q \leqslant 1$ is a (dimensionless) shape parameter. The radius R_c defines a volume inside which the density is nearly constant. Thus when $r \ll R_c$ we have once more harmonic motion of

angular frequency $\omega = v_o/R_c$. If we let $q = 1$ and define $u \equiv r/R_c$, the volume density ρ reads

$$4\pi G\rho(u) = \nabla^2\Phi_g = \frac{v_o^2}{R_c^2}\frac{3+u^2}{(1+u^2)^2} \qquad (16)$$

and the integrated mass $M_g(u)$

$$M_g(< u) = \frac{v_o^2 R_c}{G}\frac{u^3}{u^2+1} \ . \qquad (17)$$

The mass $M_g(u \gg 1) \propto u$ diverges at large distances, however this is not a serious flaw since we will consider only the region where $u \sim 1$. The mass $M_g(u = 1) = v_o^2 R_c/2G$ fixes a scale against which to compare the black hole mass M_{bh}. Since the black hole will orbit within the harmonic core, we set

$$M_{bh} \equiv \tilde{m}_{bh}\frac{v_o^2 R_c}{2G} \qquad (18)$$

with $0 < \tilde{m}_{bh} \leqslant 1$, and

$$\mathcal{M}(u) = 1 + \tilde{m}_{bh}\frac{1+u^2}{u^3}$$

bears the same meaning as before. The core radius offers a reference length to the problem. The position and velocity of the black hole at any time follow from (10), where the amplitude is set by fixing the dimensionless number $u_o = R_o/R_c$ and the angular frequency ω is

$$\omega = \frac{v_o}{R_c} \ .$$

Our goal is to quantify the time-evolution of a large number of orbits in the combined logarithmic and black hole potentials. If we pick parameters such that

$$m_\star \ll M_{bh} < M_g(\max\{u\})$$

then we may neglect the collective feedback of the stars on the black hole and galactic potential and study only the response of individual orbits evolving in the time-dependent total potential. This approach will remain valid so long as the response of the stars are relatively modest. The time-evolution of orbits was done numerically using a standard integration scheme, which we describe below.

3.1   Equations and numerics

The energy E_J of a star is computed from

$$E_J = \tfrac{1}{2}v^2 + \Phi_g(\boldsymbol{r}) + \Phi_{bh}(\boldsymbol{r}, t) \qquad (19)$$

where

$$\Phi_{bh}(\boldsymbol{r}, t) \equiv -\frac{GM_{bh}}{||\boldsymbol{r} - \boldsymbol{R}||} \qquad (20)$$

is an explicit function of time through (10); from here onward we will write (x_{bh}, y_{bh}) for the coordinates at time t of the black hole in the xy-plane. The time-derivative

$$\dot{E}_J = \partial_t\Phi_{bh}(\boldsymbol{r}, t) \neq 0$$

and hence energy is not a conserved quantity. We use this fact to define a set of six first-order differential equations

$$\frac{\mathrm{d}}{\mathrm{d}t}(\boldsymbol{r}, E_J, \boldsymbol{v}, \dot{E}_J) = (\boldsymbol{v}, \dot{E}_J, -\boldsymbol{\nabla}\Phi, F_J) \qquad (21)$$

where the time-derivatives are computed in the usual way, and we find for a black hole orbit confined to the harmonic core

$$\begin{aligned}
F_J = \ & 3\frac{GM_{bh}}{||\boldsymbol{r} - \boldsymbol{R}||^5}\left([x_{bh} - x]\widehat{[x_{bh} - x]} + [y_{bh} - y]\widehat{[y_{bh} - y]}\right) \\
& + \frac{GM_{bh}}{||\boldsymbol{r} - \boldsymbol{R}||^3}\left(\dot{x}_{bh}^2 + \dot{y}_{bh}^2 - \dot{x}\dot{x}_{bh} - \dot{y}\dot{y}_{bh}\right) \\
& - \omega^2\frac{GM_{bh}}{||\boldsymbol{r} - \boldsymbol{R}||^3}\left([x_{bh} - x]x_{bh} + [y_{bh} - y]y_{bh}\right) \ .
\end{aligned} \qquad (22)$$

The expression for F_J admits a simplification when the black hole is set on a radial orbit (10) but note that (22) is not invariant to a swap of x for y and *vice versa* when $y_{bh} = 0$.

3.1.1   Compact kernel

The potential (20) is singular when $\boldsymbol{r} = \boldsymbol{R}$ which introduces large errors in the integration. To alleviate this we redefine (20) using a compact kernel, effectively smoothing over the singularity. Let ε_{bh} be a constant length and write

$$\Phi_{bh}(\boldsymbol{\mathcal{R}}, t) = -\frac{GM_{bh}}{\varepsilon_{bh}}\hat{\Phi}(\boldsymbol{\mathcal{R}}, t), \qquad (23)$$

whenever $\mathcal{R} \leqslant 1$ where $\mathcal{R} = ||\boldsymbol{r} - \boldsymbol{R}||/\varepsilon_{bh}$. We pick a compact kernel which minimises force errors at $\mathcal{R} = 1$ (Dehnen 2003) and define

$$\hat{\Phi}(\mathcal{R}) = 1 + \tfrac{1}{2}\left(1 - \mathcal{R}^2\right) + \frac{3}{8}\left(1 - \mathcal{R}^2\right)^2 \ . \qquad (24)$$

This last equation fails when $\mathcal{R} > 1$, however this is of no concern since the gradient is continuous at $\mathcal{R} = 1$ and matches exactly the one derived from (20) at that radius. Integration of equations (21) with respectively (20), or (23) and (24), when $\mathcal{R} > 1$ or $\leqslant 1$, poses no particular difficulty, though Eq. 22 takes another form inside $\mathcal{R} < 1$ (see below).

3.1.2   Choice of units & integrator

For convenience we have chosen scales for the background potential such that $G = v_o = M = 1$. Borrowing from the case of the MW black hole, we set a kernel length $\varepsilon_{bh} = 2 \times 10^{-2}$ which will wipe out all high-deflection angle collisions, i.e., those due to orbits with little angular momentum.

We have used an explicit fourth-order time-adaptive Bulirsch-Stoer integrator taken from Press et al. (2002) for solving (21). We have performed a series of tests with a static potential by setting e.g. $\tilde{m}_{bh} = 1$ and $u_o = R_o = 0$ in (10). With these parameters $\dot{E}_J = 0$, and we checked that a precision of $1 : 10^{14}$ is maintained for a runtime of

200 units. In particular we validated Eq. 24 by integrating radial stellar orbits running through the black hole, both along the x- and y-axis. We also integrated a circular orbit at the edge of the kernel, or $\mathcal{R} = 1$, and found no indication of a drift in energy or any kind of random fluctuations.

The situation is less glorious when integrating with finite black hole motion. To see why, let us write down F_J in (21) with (10) and $\mathcal{R} < 1$. Some straight forward algebra yields

$$
\begin{aligned}
F_J &= 3\frac{GM_{bh}}{\varepsilon_{bh}^5}\,(x - x_{bh})\,(\dot{x} - \dot{x}_{bh}) \\
&\quad -\frac{GM_{bh}}{\varepsilon_{bh}^3}\left(\frac{5}{2} - \frac{3}{2}\mathcal{R}^2\right)\frac{\mathrm{d}}{\mathrm{d}t}(x - x_{bh})\dot{x}_{bh}\,.
\end{aligned}
\tag{25}
$$

Since the relative distance between the star and the black hole is $< \varepsilon$, we find that $F_J < O(1/\varepsilon^5)$ which gives $O(10^9)$ for the parameters chosen. As such this would not be problematic, however the time-steps required to maintain an accuracy of $1 : 10^{14}$ for a typical integration time become tiny, and the computer run-time, prohibitive. We found a practical solution to this problem, by imposing that the quantity $\varepsilon^3 F_J$ be integrated to a precision of $2 : 10^{12}$, so that F_J is known to six significant digits ($\varepsilon \sim 10^{-2}$). Whenever this condition was not met, we only included the orbit in the analysis *up to* that point in time, after which it was ignored. This situation occurred relatively seldom, and affected some $3 - 4\%$ of cases at most. This was so, for example, when the initial configuration either started out with many stars on near-radial orbits and small-amplitude black hole motion; or, when the black hole was allowed to flirt with a large number of stars by covering a distance comparable to or exceeding its radius of influence.

3.2   Initial conditions

We limit our exploration to the case of coplanar motion. The volume density (16) stretches to infinity and yields a divergent integrated mass. Since we are only interested in the central-most volume, we decided to keep only stars that remain inside a given radius. (A selection by energy E_J would be equivalent.) Our model calculation of §1 had shown that the response of the star to black hole motion is a strong function of the ratio of their orbital periods. The orbital period of the star is $\propto 1/\sqrt{G\overline{\rho}}$, where $\overline{\rho}$ is the mean volume density inside the semi-major axis of the orbit. These two observations combined suggests that we only include orbits out to where the density varies most rapidly. We chose a truncation radius such that $u_t \leqslant e$, close to the value $2.80(7)$ at which $\mathrm{d}\ln\rho/\mathrm{d}\ln r = -2.101..$ reaches a minimum.

We now specialise to the case of circular orbits in the axisymmetric potential Φ_g by setting $q = 1$ in (15). Positions are attributed by Monte Carlo method using the density as probability distribution. The square circular velocity at each radius is

$$
\left(\frac{v_c}{v_o}\right)^2 = \frac{u^2}{u^2 + 1} + \frac{\tilde{m}_{bh}}{2u}
\tag{26}
$$

and the sense of motion chosen randomly so that the to-

tal angular momentum of the stars is zero to within root-n noise. The energy may be written as

$$
\frac{2E_J}{v_o^2} = \ln|u^2 + 1| + \frac{u^2}{u^2 + 1} - \frac{\tilde{m}_{bh}}{2u}\,.
\tag{27}
$$

This expression is easily differentiated to yield an analytical form for $E_J' = \mathrm{d}E_J/\mathrm{d}u$ which is the density of states of stars of energy E_J at u. Since we are only interested in coplanar orbits, the mass element drawn from (16) is

$$
\delta M = 2\pi R_c^3 \rho(u) u \mathrm{d}u \equiv f(u)\,\mathrm{d}u = f(u)\frac{\mathrm{d}E_J}{E_J'} \equiv f(E_J)\mathrm{d}E_J
$$

where the energy distribution function $f(E_J)$ is known in parametric form,

$$
f(E_J) \equiv \frac{R_c v_o^2}{G}\frac{u^3\,(3 + u^2)}{\tilde{m}_{bh}(u^2 + 1)^2 + 4u^3\,(u^2 + 2)}\,.
\tag{28}
$$

This equation shows that when $\tilde{m}_{bh} = 0$ (no black hole) we find $f(E_J) \to$ constant in the limit $u \to 0$; and $f(E_J) \propto u^3$ in the same limit when $\tilde{m}_{bh} \neq 0$. Thus the bulk of the stars avoid the central black hole. Equation (28) will be helpful when assessing the noise level of the response of the stars to black hole motion.

4   Results

We have until now fixed the gravitational constant $G = 1$ and velocity scale of the galactic potential $v_o = 1$. The initial conditions require further that we fix the black hole mass parameter $\tilde{m}_{bh}$ in (18), black hole's amplitude of motion u_o, and the core radius, R_c. The total mass (17) will integrate to 1 up to $u_t \simeq e$ if we set $R_c \simeq 0.46$. This fixes all scales in the problem, and we note that $\approx$ half the stars lie inside R_c, and an equal fraction outside. The black hole's radius of influence is obtained in terms of $\tilde{m}_{bh}$ from equating (17) to (18). The result is shown on Fig. 4. We use this relation to set a more stringent constraint on the motion of the black hole by imposing that it orbits always within its radius of influence, an improvement on our initial ansatz that $u_o < 1$, since (10) is a better solution to the black hole's orbit closer to the origin.

4.1   Reference case, $\tilde{m}_{bh} = 0.3$

We set up a reference case inspired by MW data which will guide us through our exploration of parameter space. Since the MW black hole lies close to the galactic centre at a velocity $\simeq 2 - 4$ km/s this suggests that we focus on cases where the black hole remains well inside the central core. We pick a black hole mass equal to 30% of the core mass, $\tilde{m}_{bh} = 0.3$, and set an upper limit of $u_o = 0.66$ on its amplitude of motion, when it would exceeds slightly its influence radius of $\simeq 0.57$ (Fig. 4).

To see how orbits respond as u_o is increased from zero, we draw on figure 5 Poincaré sections of a single orbit for four values of u_o : $0, 0.15, 0.33$ and 0.66. The case of a fixed black hole is shown on Fig. 5(a), when the star describes a circular orbit of radius $r = 1.78$ which is $\gtrsim 3$ times the influence radius of the black hole. The orbital
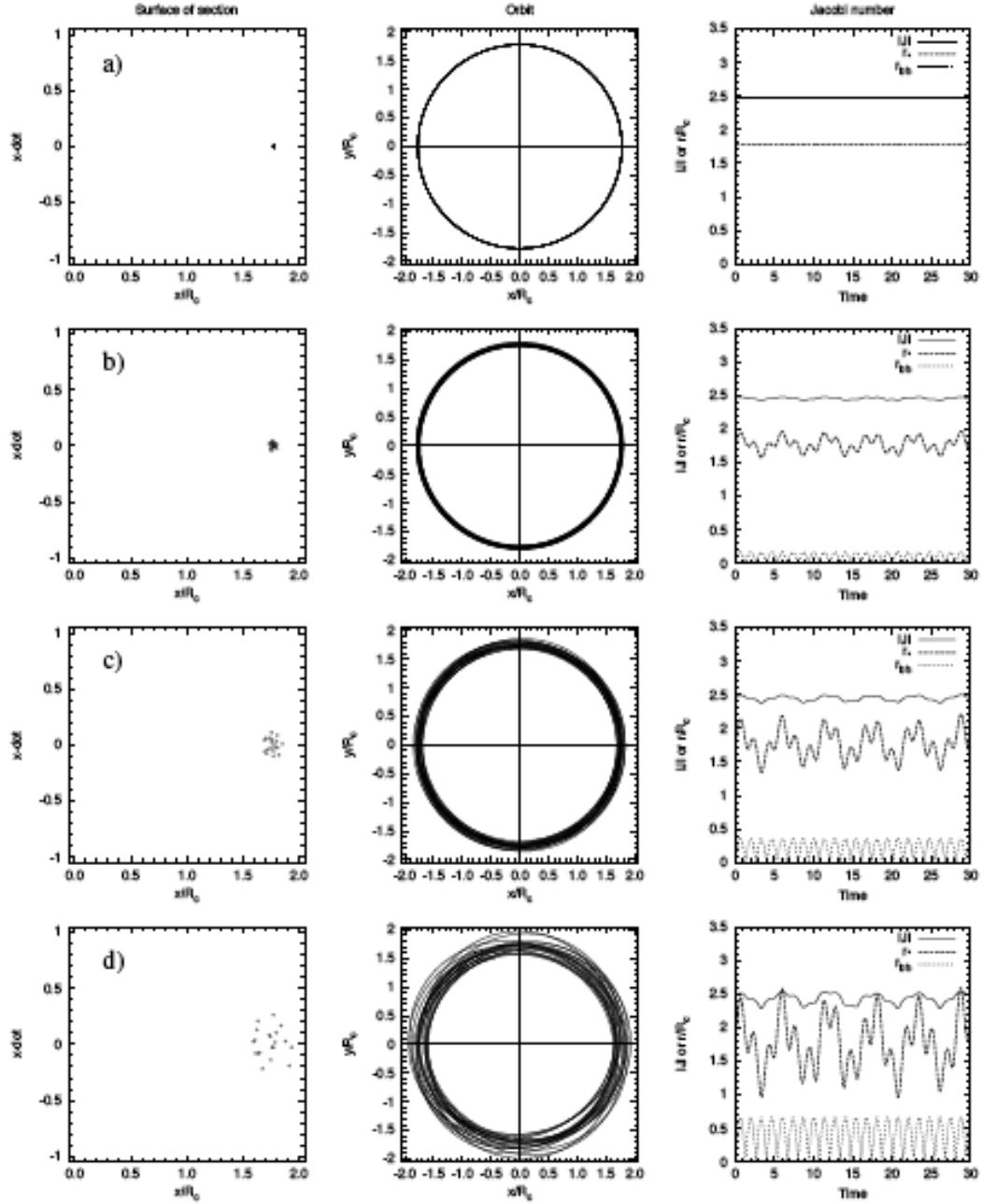
Figure 5. Poincaré section $(\dot{x}, x)$ at $y = 0$ (left panels), orbit (middle) and radii and energy (right) for a single stellar orbit in the logarithmic potential to which we added an $\tilde{m}_{bh} = 0.3$ black hole. The panels to the right display the binding energy of the star (solid line) along with the distance $r_\star$ of the star to the black hole (dash). Modulations in energy match one to one variations in $r_\star$. The black hole orbit r_{bh} (dots) is also displayed for comparison. The four rows show the orbit for different values of u_o: a) 0.0, b) 0.15, c) 0.33 and d) 0.66.
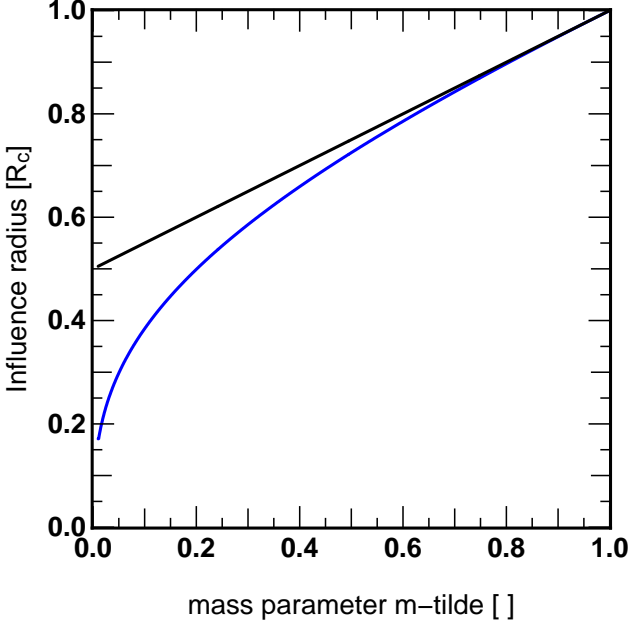
Figure 4. Influence radius in units of R_c as a function of the mass parameter $\tilde{m}_{bh}$ defined in (18). In the limit $\tilde{m}_{bh} \to 0$ the radius $\propto \tilde{m}_{bh}^{1/3}$ rises rapidly. In the neighbourhood of $\tilde{m}_{bh} = 1$, the radius $\propto \tilde{m}_{bh}$; the straight line is the curve $\tilde{m}_{bh}/2 + \frac{1}{2}$.

Table 1. Initial conditions of the numerical orbit integrations. The influence radius r_{bh} defined in (5) is given in computational units. The potential (15) is defined in units such that $G = v_o = 1$. The core radius $R_c = 0.459$, and the truncation radius $r_t \simeq 2.53$ gives an integrated mass (17) = 1.

Circular stellar orbits ('cold')			
Name	$\tilde{m}_{bh}$	u_o	r_{bh}	Comment
		$[R_o/R_c]$		
C1	0.30	0.00	0.258	Static
C2	0.30	0.07	0.258	
C3	0.30	0.15	0.258	Reference case
C4	0.30	0.21	0.258	
C5	0.30	0.30	0.258	
C2s	0.15	0.15	0.197	Shadows C2
C3s	0.15	0.30	0.197	Shadows C3

'Warm' or 'Hot' runs			
Name	$\tilde{m}_{bh}$	u_o	r_{bh}	Comment
		R_o/R_c		
W1	0.30	0.15	0.258	
W1c	0.30	0.15	0.258	circular BH orbit
H1	0.30	0.15	0.258	
W2	0.30	0.21	0.258	

period $= 2\pi r/v_c = 11.18$ and the integration was for a total of 200 time units (18 revolutions). The middle- and right panels show the orbit and the star's energy (solid curve) and distance to the black hole (labeled $r_\star$, dashed curve), respectively. Fig.5(c) illustrates the situation when the black hole motion has amplitude $u_o = 0.33 \simeq 0.58\times$ its influence radius. The star's orbital radius now varies from

a minimum of approximately 1.65 and up to 1.85, a gap of $\approx 10\%$ compared to the circular orbit; the same conclusion applies to the cycles seen in binding energy (right panel, Fig. 5[c]). We note that the modulations in E match one to one the profile of $r_\star$, which is an indication that a strong coupling is still operative even for stars orbiting well beyond the black hole's radius of influence. The scatter seen in the Poincaré sections of both Fig. 5(c) and (d) confirms this view, and suggests that the original circular orbit becomes mildly chaotic (no loop or resonant structure).

The response of individual orbits to black hole motion would leave a measurable trace only if their signal rises above the background noise of other orbits that may be otherwise affected. We sought out a relation between an unperturbed and time-independent distribution function and the noise level of a discrete realisation of that function with N bodies. The reference distribution function is given by (28) which we discretised using 100 equal-size bins of width $\Delta E \simeq 0.07$. This curve is plotted as a histogram on Fig. 6. We then measured the root-mean square differences with the analytic distribution function by drawing different numbers of orbits in the range 10,000 to 100,000. The results are shown for four values of N on Fig.6(a-d). We find the rms differences drop to $\sim 4 - 5\%$ already for $N \gtrsim 40,000$, comparable to Poisson noise (roughly $1/\sqrt{400} \simeq 5\%$ fluctuations per bin). For completeness, we also plot the relative differences in percentage at each bin of energy on the rectangular frames below each panel. This relative energy error is dominated by low-number statistics and becomes very large when $E \lesssim -1$, which, for our choice of parameters, corresponds to a radius $u \simeq 0.074$ enclosing $\simeq 0.02\%$ of the total mass (expected Poisson noise of $\approx 20\%$). The error made in dropping orbits below that level of energy from our analysis is of the same order. Furthermore, stars that are that close or closer to the origin would be trapped by the black hole gravity and remain on high-velocity Keplerian orbits around it. This would remain true even if the black hole were set in motion at a comparatively small velocity. Such orbits are not the focus of this work.

Figure 7 compares the energy distribution function of a set of 93617 orbits when the black hole is set in motion with amplitude $u_o = 0.33$, to the initial distribution function, when the black hole sits at the origin. Recall that this latter distribution would be time-independent. The orbits were all integrated for $t = 20$ unit of times, which corresponds roughly to 10 revolutions at the edge of the system. The energy axis is once more split in 100 bins, and we find once more an rms noise level of $\approx 4\%$. Let us take as one standard deviation a difference of 5% with the analytic function (28). The signature of black hole motion seen on Fig. 7(b) leaves four peaks of more than three standard deviations, and ten with one or more standard deviations, all to the left of $E = -1$. The most significant peak at $E \simeq 1.31$ has an amplitude of $+29\%$, or five standard deviations. This corresponds to a circular orbit at radius $u = 1.169$ ($r = uR_c \simeq 0.5355$ units), which is ~ 2 times the black hole radius of influence (cf. Fig. 4) and 3.57 times its amplitude of motion, u_o. This is clearly an indication of energy exchanges through beat frequencies, i.e., resonances.
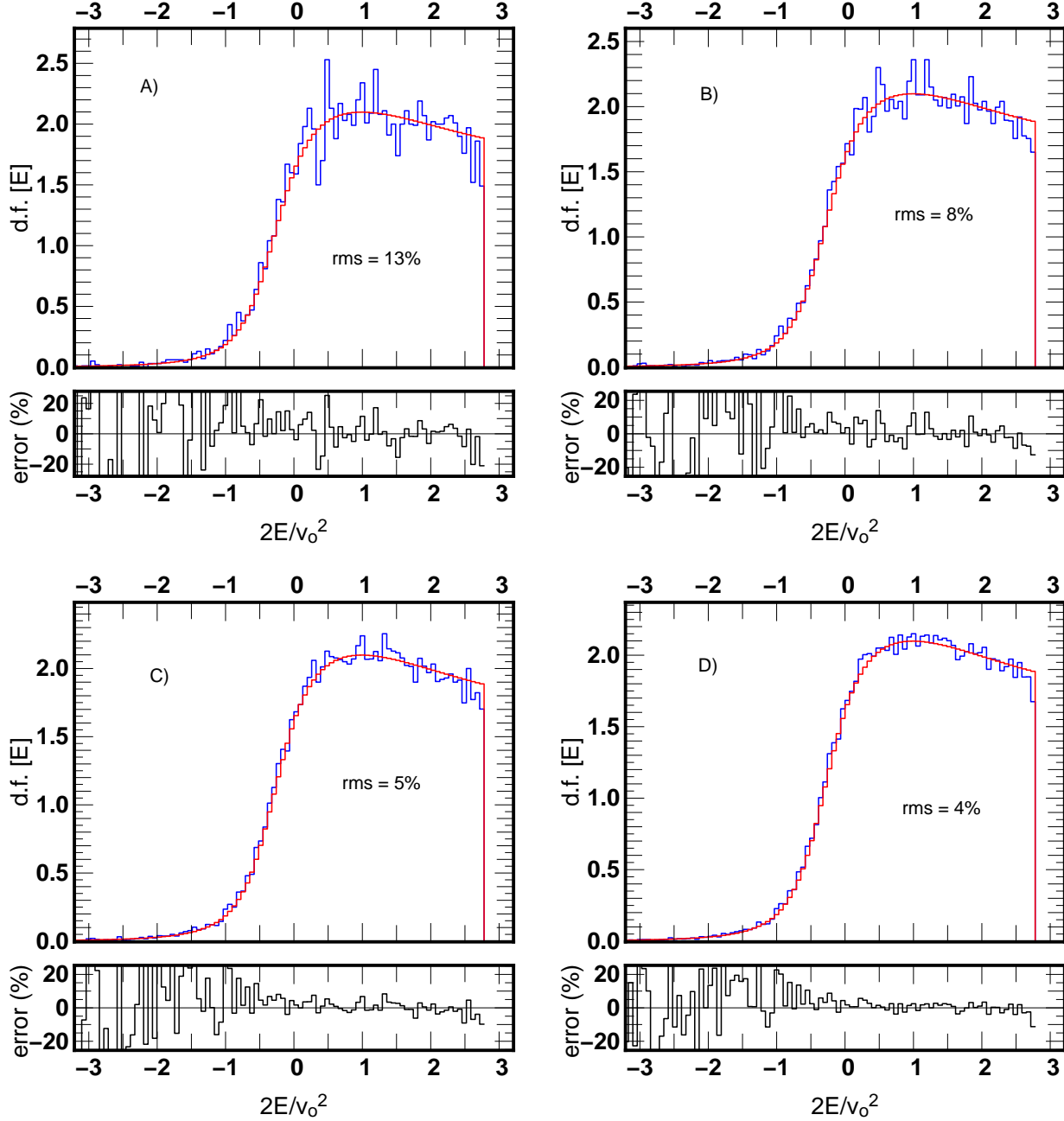
Figure 6. The energy distribution function (d.f.) for four discrete realisations with (from [a] to [d]): $N = 10,000, 20,000, 40,000$ and $80,000$ orbits. In each case the span in energy was divided in 200 bins of equal size. The analytic curve (28) is displayed as the more regular histogram on each panel, and the root-mean square differences given. The rectangular frames gives the relative differences (in %) for each bin.

4.2   Orbital resonances

To gauge the importance of orbital resonances we identify first the radius and energy of commensurate orbital periods. If we call ω' the orbital angular frequency of a star on a given orbit of energy E, then we need solve the equation

$$\nu^{-2} = \frac{1}{u^2 + 1} + \frac{\tilde{m}_{bh}}{2u^3} \equiv \left(\frac{m}{n}\right)^2 \qquad (29)$$

where $\nu = \omega/\omega'$ as in §1, which requires solution for all prime integer ratios m/n. The above equation could be set in terms of $\mathcal{M}$ defined in (9) as done in (12) in the case of a harmonic potential. Instead we solve for E, u from (29), and classify the result as a Keplerian resonance when the corresponding value for $\mathcal{M} > 2$, which will always be the case when $m > n$, and a Galactic resonance for all other cases $m \leqslant n$. Table 2 lists the results for a broad range of values of $m : n$. Remarkably, the energy level of *Galactic* resonances match almost exactly the apparent nodes in
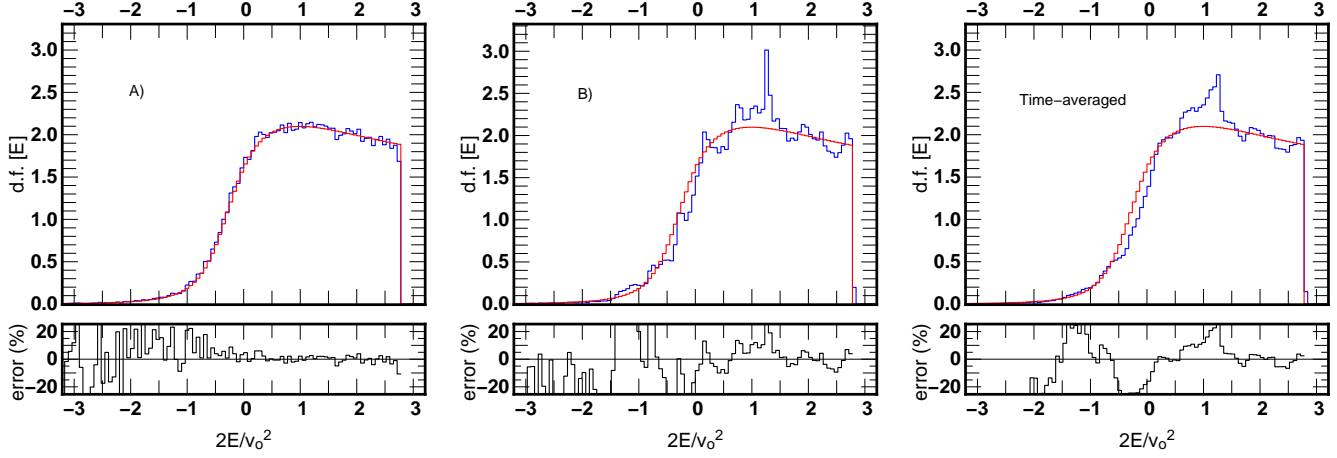
Figure 7. Energy distribution for two configurations: A) static black hole at the centre of coordinates; B) black hole on a radial orbit of amplitude $u_o = 0.33$, after 20 time units of evolution. In both cases the mass parameter $\tilde{m}_{bh} = 0.3$. The energy d.f. averaged over five output times is shown on the right-hand side for comparison. The smooth histogram on all three panels was constructed using (28).

Table 2. Orbital resonances defined in (29) for several values of the commensurate ratio $m : n$. Results for $m \leqslant n$ (or, $\mathcal{M} \geqslant 1$) are labeled Galactic, otherwise they are labeled Keplerian ($\mathcal{M} < 1$).

Galactic	u	r	$2E/v_o^2$
$m : n$			
1:1	0.748		0.602
2:3	1.292		1.490
3:5	1.479		1.744
1:2	1.849		2.178
2:5	2.390		2.691
1:3	2.918		3.097

Keplerian	u	r	$2E/v_o^2$
$m : n$			
11:10	0.663		0.443
6:5	0.598		0.317
4:3	0.532		0.187
13:9	0.489		0.101
3:2	0.471		0.064
5:3	0.427		-0.031
2:1	0.364		-0.171
5:2	0.304		-0.320
3:1	0.265		-0.433

the energy distribution function seen on Fig. 7(b). This is in close agreement with our analysis of §1, when we argued that commensurate values of ν would give no net work after an integer number of black hole revolutions. This is not the whole picture, however, since the binding energy of individual orbits is constantly changing in time, with as many stars gaining energy as those losing energy. Hence one may think of the energy d.f. of Fig. 7(b) as a standing wave modulated by small sinusoidal modes propagating at a finite pattern speed. A clearer picture emerges once we compare Fig. 7(b) to a time-averaged d.f. for the same system. On the right-hand panel of Fig. 7, we graph the average of five energy distributions functions sampled over a time span of $t = 13$ to 17. This corresponds to $4/\omega = 4R_c/v_o \approx 2$ full black hole oscillations. In total 468115 orbits were put to contribution. Comparing this curve to the one displayed on Fig. 7(b), we find fewer peaks exceeding one standard-deviation. The smoother appearance of the distribution function supports

the interpretation of sine-like oscillations on Fig. 7(b) as transitory features. Thus we expect phase-mixing to erase such features on a dynamical time-scale. By contrast, the two broad peaks at $2E/v_o^2 \approx 1$ and -0.5 remain, their amplitude hardly dented by the time-averaging. These peaks should, therefore, leave observable features in kinematic- and density maps.

This intuition is confirmed, at least partially, by a Poincaré section of (x, v_x) in the plane $y = 0$. On Fig. 8 we graph the surface of section of 500 orbits, each evolved for twenty time units. The number of points varies between orbits from ~ 10 and up to 200, according to the period. We observe large but localised scatter in the velocities as a function of $u_x = x/R_c$. The vertical full line at $u_x \simeq 0.3$ indicates the amplitude of motion of the black hole, while the dash lines are the location of resonances listed in Table 2. The scatter decreases rapidly as we move to large radii. Specifically there is a sharp drop as we reach beyond the 1:1 resonance, and thereafter significant scatter is centered around $u_x \approx 1.6$ and 2.5. These values of u_x correspond to energies of $2E/v_0^2 \approx 1.9$ and 2.8, respectively, matching the features seen on the energy distribution function (cf. Fig. 7). The broad peaks seen on graphs of the energy d.f. falls inside the 1:1 resonance and are lost in the scatter on Fig. 8.

4.3 Surface density, velocity maps

Maps of the surface density and velocity field are of interest. The configurations are isotropic initially when the black hole starts off at the centre of coordinates. At later stages neither the density nor the velocity fields respect this initial property. We toyed with the idea of plotting both surface density Σ and velocity field in cylindrical coordinates centered either on the system's centre of mass, or the black hole. This turned out to be useful only when both coincides, which will only occur when the black hole is on a radial orbit. Instead, we opted to map out both quantities on a uniform Cartesian grid. This has the advantage of an unbiased linear resolution over all space and is identically suited to any type of black hole orbit (radial, circular or other). The surface density is obtained at any time by a simple count-in-cell
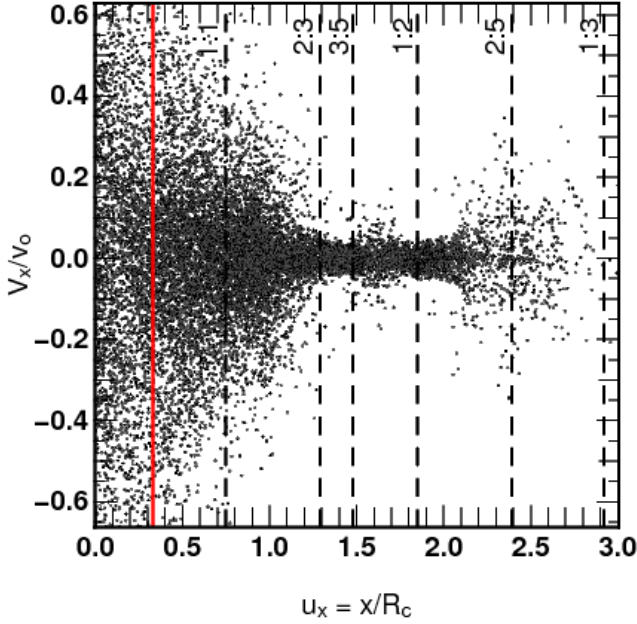
Figure 8. Surface of section in the $y = 0$ plane showing v_x in units of v_o as a function of $u_x = x/R_c$. The dashed vertical lines indicate resonances listed in Table 2.

(CIC) technique. No smoothing or averaging of neighbouring cell has been performed. Density profiles and their significance should be interpreted with due consideration to root-n noise: a typical grid would have 30×30 mesh points, and hence a mean count per cell of at least $\gtrsim 4\,10^4/900 \simeq 44$, which translates to relative fluctuations of 15%. In practice we have used on order 10^5 orbits, and so the noise level always falls in the range 10% - 15%. As we will see, the density fluctuations that we measured at times exceeded 60% of the reference initial profile, giving a signal-to-noise ratio of at least 4 and perhaps as high as 7.

4.3.1 Flat-fielding the velocity map

The initial velocity (26) is known at any point in space, however it is set in the centre of mass reference frame. Since we wish to map out velocities on a Cartesian grid, we must be cautious to compute the expected mean velocity in any cell for comparison. This poses a problem around the origin of coordinates, when the radius $\sim$ a few grid cells only. Calling δu the grid size, we find from (26) an absolute error on v_c of

$$\frac{|\delta v_c|}{v_c} \leqslant \left(\frac{|\delta u|}{2u}\right) \left| \frac{2}{1 + u^2} + \frac{\tilde{m}_{bh}}{2 \max\{u, \varepsilon\}} \frac{1 + u^2}{u^2} \right| \quad (30)$$

which becomes large when $u \lesssim \delta u$. We then compute (30) for each orbit falling inside a given mesh and take the average square difference with the local circular velocity:

$$\frac{1}{n} \sum_{i=1}^{n} \left(\frac{||v|| - v_c}{1 + |\delta v_c|/v_c} \right)^2 \equiv \sigma^2 \quad (31)$$

where the sum is over all n orbits inside the mesh at time t obtained by CIC. This gives a direct measure of the local dispersion as a result of black hole motion, and a reference map to eliminate noise when the black hole is fixed. For that case, we find using (31) residual errors not larger than $1 : 10^4$ or 0.01 %.

4.3.2 Time sequence

We graph on Fig. 9 the time-sequence of the surface density and dispersion σ for 93607 orbits integrated over 20 time units. The figure shows two sets of two rows, regrouped to help match features seen in the density, to those seen in de velocity field. Initially the orbits are isotropic and circular, which explains the two feature-less frames at the top-left corner of Fig. 9. At subsequent times, the plots show very pronounced and fast-evolving features, both in maps of the density and velocity. The scale of surface density was chosen to identify peak density enhancements of 60% when compared to the initial profile. The core radius $R_c \approx 0.45$, nearly twice the black hole influence radius of $\simeq 0.56R_c$, is displayed as the dashed circle. Inside and up to that radius, the mass profile shows arcs, bubbles and other transient features, all suggestive of unsteady, perhaps chaotic, orbital motion. Outside that radius, we find more steady, ring-shaped features which match the position of resonances (Table 2).

By comparison, the relative velocity dispersion peaks at $\approx 25\%$ of the local circular velocity v_c. Not surprisingly, the largest deviations in velocity nearly always coincide with the position of the black hole (red dots on Fig. 9). The most remarkable features on these frames are the large dispersions measured well outside the core radius. A particularly striking sequence runs from $t = 15$ to 17, when a large arc seems to close up on itself in the region $x \approx -0.75, y \simeq 0$. This large dispersion is found at a distance some 5 times larger than the amplitude of the black hole's orbit. If we scaled these features to the MW, then an anomalous local velocity dispersion would be expected up to from 3 to 4 pc away from Sgr A⋆. In conclusion, the black hole has a very strong impact on circular orbits, both in terms of spatial features and kinematics, up to ≈ 2 to 3 times its radius of influence (see also Fig.8).

4.4 Projected velocity field

The line-of-sight velocity offers a direct way to measure the effect of black hole motion. Our strategy, then, is to apply a slit of some 100 mesh running across the x- and y−axis (viewing angles of 0° and 90° to the black hole orbit, respectively), and compute both the integrated one-dimensional velocity and the square velocity dispersion at each mesh point. The expected velocity in projection $v_{1d}(x$ or $y) = 0$ for isotropic initial conditions. The analytic calculation of the dispersion σ_{1d} proceeds straightforwardly from (16) and (26). Inspection of several time frames, using either x or y as the line-of-sight, revealed no significant deviation from the profile derived for circular motion, at any point of evolution. Specifically, we looked for asymmetries in the dispersion when comparing the two viewing angles, but found none (to within $\approx 2\times$ the noise level). Consequently we dis-

Figure 9. Time-sequence showing the surface density Σ and flat-fielded velocity dispersion σ for a system with an $\tilde{m}_{bh} = 0.3$ mass black hole on a radial orbit of amplitude $u_o = 0.33$ ($R_o \approx 0.15$). The frames show maps of Σ (first and third rows) and dispersion σ (second and fourth rows) at times $t = 0, 13, 14, 15, 16$ and 17 units. The black hole is shown as a red dot, while the cross is the origin of coordinates. The black arrows are the local net angular momentum, which remains at the root-n level everywhere.
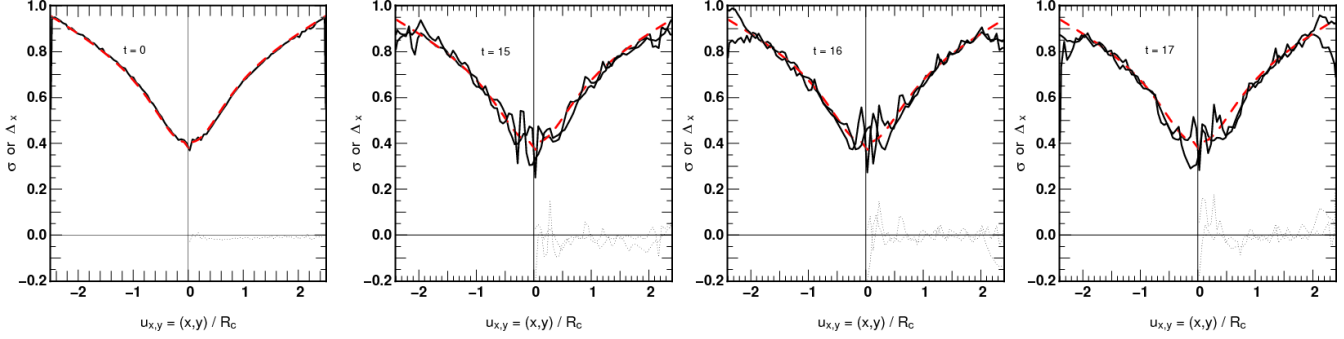
Figure 10. Time-sequence showing the line-of-sight root-mean-square velocity dispersion, σ, for the reference case of $\tilde{m}_{bh} = 0.3 \simeq u_o$. A total of 100 bins were used for two viewing angles, down the x- and y-axis, in each case. At $t = 0$ (panel to the extreme left) the analytic expectation with a black hole at the centre of coordinates is well recovered from 69773 circular orbits. The dashed line shows the theoretical expectations which drops to zero at the origin (all motion is orthogonal to the line-of-sight). The solid line gives the dispersion recovered from summing over all orbits. When $t > 0$, σ differs from the expected value up to $u_{x,y} \simeq u_o$, the black hole amplitude of motion. At large distances, the broken curve suggests Poisson noise from small-N statistics. The thin dotted lines are the differences about the coordinate centre $\sigma(u) - \sigma(-u)$ for each line-of-sight.
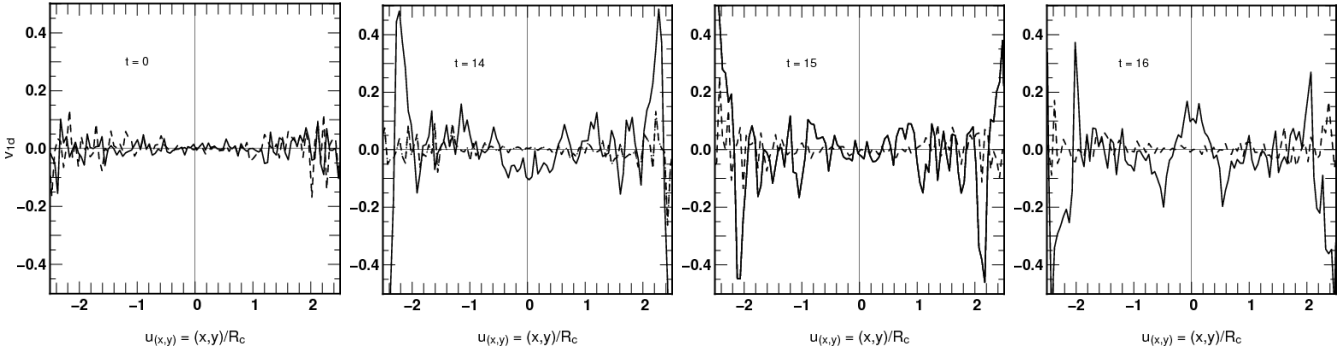

Figure 11. Time-sequence showing the line-of-sight mean velocity for the reference calculation with black hole mass $\tilde{m}_{bh} = 0.3$ and amplitude $u_o = 0.33$. The velocity was measured when looking down the x-axis (solid line) and the y-axis (dashed line). The x-axis data show cyclical variations with a peak signal-to-noise ration inside $u = 1$ (or, $r = R_c$).

carded runs of σ_{1d} from analysis. (In §5 we comment on the dispersion in the context of fragmentation modes.)

The situation with v_{1d} is more profitable. Fig. 11 graphs the line-of-sight velocity for three time frames of the reference C3 calculation with $\tilde{m}_{bh} = 0.3$ and amplitude $u_o = 0.33$. The results are shown for two viewing angles in each case at times $t = 0, 14, 15$ and 16. A total of 83697 orbits were binned on a mesh of 100 points. The Poisson fluctuations $\sim 3\%$ on average but are less than 1% inside $|u| < 1$, and $\approx 10\%$ near the end-points due to sampling effects. Looking down the y-axis orthogonally to the black hole orbit, we find $v_{1d} = 0$ everywhere to root-n noise, a result which confirms the intuition that the y-component of the velocity field preserves the initial symmetry through the $z - x$ plane (Fig. 11, dashed lines). A sample of these three and two more frames gave very similar results for the root mean-square scatter $\sqrt{<\delta v_{1d}^2>} \simeq 0.002$ when averaged over the mesh.

When we switch lines-of-sight, we find large time-

dependent oscillations of v_{1d} of a half-period $\simeq 2$, close to half the orbital period $= 2\pi R_c/v_0 = 2.9$ of the black hole (Fig. 11, solid line). This highlights a close relation between the stars' angular momentum $L_z = xv_y - yv_x$ and the phase of the black hole orbit: the torque $\Gamma_z \approx GM_{bh}/r^2 (y_\star/r)(x_\star - x_{bh})\hat{z}$ (where $r = ||\boldsymbol{r}_\star - \boldsymbol{r}_{bh}||$ is the distance between the star and the black hole) will be positive for half the stars inside a given mesh centered on $y_\star$. This torque, then, will give a boost to the momentum of stars when $\Gamma_z \cdot L_z > 0$ (otherwise the torque will oppose the star's momentum, and decrease its magnitude). As a result the line-of-sight velocity does not integrate to zero and shows cyclic variations with u_y. Inspections of the same five frames as before using the x-axis as line-of-sight showed that $|v_{1d}|$ varied from 0.008 to 0.034 with a root mean square scatter $\sqrt{<\delta v_{1d}^2>} \approx 0.03$. The run from $t = 14$ to 16 is an example of a sequence during which $|v_{1d}|$, averaged over all bins, goes from 0.032, to a minimum 0.004, and then back to 0.034. We stress that the trend with time is averaged over

Table 3. Results for the models listed in Table 1.

	Circular stellar orbits ('cold')			
Name	rms $(2\delta E/v_o)^2$	rms $(\delta v_{1d}^2)/v_o$		Comment
	$\pm 4[\%]$	x-axis	y-axis	
C1	0	0.015	0.015	$t=0$ data
C2	12 ± 2	0.022	0.020	
C3	29.2	0.071 ± 0.01	0.042	Ref. case
C4	36.9	0.044	0.026	
C5	51	0.038	0.024	
C2s	24	0.025	0.021	Shadows C2
C3s	50	0.041	0.022	Shadows C3
	'Warm' or 'Hot' runs			
Name	rms $(2\delta E/v_o)^2$	rms $(\delta v_{1d}^2)/v_o$		Comment
	$\pm 4[\%]$	x-axis	y-axis	
W1	18.8 ± 1.6	0.050	0.015	
W1c	22.0	0.041	0.031	circ. BH orbit
H1	28.5 ± 3.5	0.034	0.014	
W2	32 ± 1	0.033	0.016	

all bins; it is therefore of a much larger amplitude than the scatter seen inside $|u_y| = 1$. Alternatively, we may compute the ratio of $|v_{1d}|$ measured down one axis, to the values obtained for the initial configuration at $t = 0$. We find a scatter $\sqrt{<\delta v_{1d}^2>} \approx 0.015$ averaged over all bins, but only ≈ 0.005 inside $|u| = 1$ owing to better statistics. If we refer to these data as noise, then the signal-to-noise ratio when $|v_{1d}|$ goes through a maximum reaches 10 near $u \approx 0$ at these times. The rms scatter of x-axis data is systematically $\approx 3\times$ higher that of y-axis data, at all times (Table 3).

The impact of black hole motion on the distribution of angular momentum L appears clearly on a graph of the momenta distribution function. The panel to the top left on Fig. 12 (labeled 'cold') shows the d.f. at time $t = 17$ for the reference calculation, compared to the initial profiling (thin dashed line). The angular momenta are distributed in a highly symmetrical fashion about the $L = 0$ axis. Each feature marking a departure from the initial distribution is matched pair-wise for the same value of $|L|$. Thus the sum of all stellar momenta remains constant. Fig. 12 (top, left-hand panel) illustrates the rôle of the black hole acting as a catalyst to transfer angular momentum, as well as energy, to the stars.

4.5 Exploring different configurations

4.5.1 Changing the velocity field

Our choice of circular orbits has some bearing on the outcome of the calculations. In this section we assess to what extent features seen on Fig. 9 are specific to our choice of initial conditions.

To that end, we first took the same set of orbits but modified initial velocities by $\pm 10\%$ in magnitude, so that the orbits were no longer circular initially. This exercise produced similar features in the maps of density and velocity as for the reference setup, a hint that the initial response of the stars, and the general features, are not sensitive to imposing strict circular motion to the initial conditions. We then toyed with the idea of computing a velocity field consis-

tent with the logarithmic potential based on moments of the Boltzmann equations (e.g., Binney & Tremaine 1987). Doing so however would have meant introducing a new energy d.f. and made comparisons with the case of circular orbits more difficult. Instead, we opted to keep the same energy d.f. and to change the velocity field by reorienting the velocity vectors randomly inside some angle chosen in the interval $\pm\theta$; here $\theta = 0$ gives the original d.f. with all orbits circular. Two new configurations were setup, one with $\theta = \pi/4$ (giving a cone of opening angle 45°), which we label *warm*, and a second with $\theta = \pi$ (fully random in azimuth), which we label *hot*. The distributions were otherwise unchanged from the reference model C3. The full list of model parameters is given in Table 1.

The results are summed up graphically on Fig. 12. The top three rows show the angular momentum d.f. (left-hand panels), the surface density (middle) and v_{1d} for two projection axis (right-hand panels) in turn for the 'cold' configuration of circular orbits, the 'warm' and 'hot' initial conditions. All data shown on the figure were taken at time $t = 17$ so the black hole assumes the same position and velocity in each case. The rings seen in the surface density map of the cold run outside $r = R_c \approx 0.5$ (shown as a dashed circle) have disappeared, and only the strongest feature inside R_c remains visible for warm and hot initial conditions. Thus the filamentary structures seen on Fig. 9 are attributable to the strong response from circular and near-circular orbits. These would make up a small fraction of warm and hot distributions. In these two cases, the number of low-L orbits is higher and more stars visit the central region on eccentric orbits. These scatter off the black hole effectively and acquire large angular momenta, a feature which can be measured up from the swelling of the momentum d.f. for large $|L|$ and the depletion of the d.f. around $L = 0$ (Fig. 12, left-hand panels, 2nd and 3rd row). The black hole motion has $u_o = 0.15$ translating to $r = 0.069$ and a radius of influence $\simeq 0.23$. Therefore all stars with an initial angular momentum lower than $r \times v \approx 0.34$ would come within a distance $\lesssim r_{bh}$ of the black hole in one revolution[3]. Fig. 12 shows this estimate in good agreement with the numerical computations. A fraction of stars concerned is about 12% in the 'warm' calculation, but close to 25% in the 'hot' run, when circular orbits have all but been wiped out.

Although details of the density and angular momentum profiles are much affected in the new configurations, compared to the reference cold one, the same does not apply to the line-of-sight velocity. The response of stars for both warm and hot computations show a distinct signature of black hole motion in the sense that once again v_{1d} fluctuates significantly more when measured down the axis parallel to the black hole's orbit. The averaged scatter in both the cases compares well with the data for the cold configuration of circular motion, at least in the interval from $u = 0$ to $|u| = 1$, or roughly two times the black hole radius of influence (Fig. 12 and Table 3). In conclusion, the black hole motion still imprints the kinematics of both warm and hot configurations, albeit to a lesser degree than for the case when stars are on circular orbits.

---

[3] We have set $r = 0.23 + 0.069$ or $u = 0.65$ and $v(u)$ from (26).

Figure 12. This graphs from left to right: the angular momentum distribution, the surface density, and the line-of-sight velocity for four models. The top row gives the results for the reference C3 calculation; the second row is the 'warm' W1 calculation; and the third row is the case H1 of a 'hot' distribution (see Table 1 and §4.5 for details). All quantities were analysed after $t = 17$ time units of integration; a minimum of 93 000 orbits were used to sample each of the parameters. The last row at the bottom gives the solution for the case W1c of a black hole set on a circular orbit. Note the strong $m = 0$ mode on the map of the surface density.
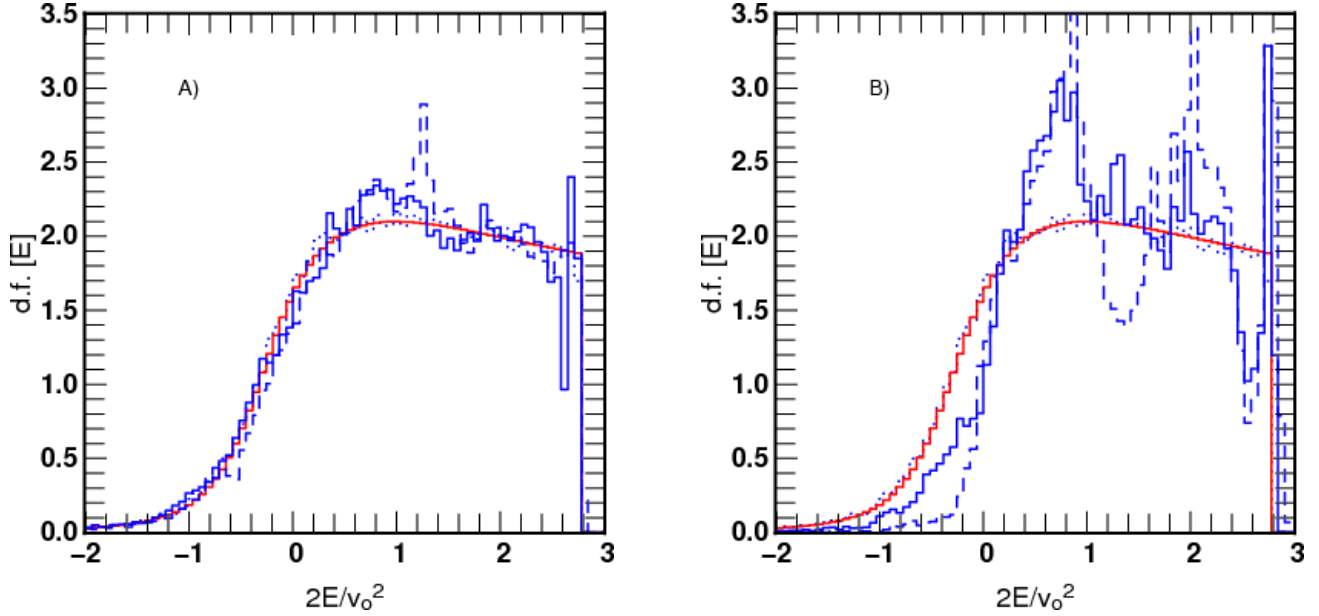
Figure 13. This graphs the energy distribution for four values of the black hole's amplitude of motion $u_o = R_o/R_c$. The dimensionless mass parameter $\tilde{m}_{bh} = 0.3$ in all the cases. On panel (a) we plot two solutions with $u_o = 0.07$ (solid line) and 0.15 (dashed line); on (b) we set $u_o = 0.21$ (solid) and 0.30 (dashed). The smooth curve is the analytic solution (28). The dots shows a discrete realisation with 69977 orbits and $u_o = 0$ (axially symmetric potential).

4.5.2 Changing the black hole parameters: scaling

Equations (11), (17) and (18) may be combined to give a proportionality relation between the work W and black hole amplitude of motion and mass function $\mathcal{M}$. Keeping only the radius-dependent terms we find

$$W \propto \frac{u_o}{u^2} \left[\tilde{m}_{bh} + \frac{u^3}{u^2 + 1} \right] \tag{32}$$

so that the ratio $W/(u_o\tilde{m}_{bh})$ is roughly homogeneous in $1/u^2$ whenever $u^3 \ll 1$. This limit would allow to retrieve a scaled version of any calculation following a redefinition of the black hole mass and/or amplitude of motion by a suitable rescaling of the lengths. However the limit $u \ll 1$ implies that the orbit is well inside the black hole radius of influence. Only a very small fraction of orbits will be found there. Nevertheless, (32) suggests that two configurations with $u_o\tilde{m}_{bh}$ kept constant would yield a similar net work W on some orbits and so possibly the same or comparable imprint on the stellar energy d.f.

We investigated this with two configurations, C2s and C3s, tailored to shadow runs C2 and C3 (cf. Table 1). The two 'shadow' runs both had a black hole mass equal to half that of C2 and C3, however twice the amplitude of motion u_o. Table 3 lists the root mean square deviations of the energy d.f. compared to the analytic curve (28). The impact on the energy distribution function is clearly stronger for the large-amplitude black hole runs. The energy deviations of 24% are nearly as large for an $\tilde{m}_{bh} = u_o = 0.15$ configuration as those obtained with the same configuration but with $\tilde{m}_{bh} = 0.30$, for which we found 29% deviations on the mean. In practice, we find that the energy fluctuations scale

almost linearly with the black hole's orbital radius u_o, a conclusion which we reached by comparing the results for cases C1 to C5. What is more, the amplitude of the response of the stars appears robust to details of the velocity field, as seen when comparing configurations with warm or hot stellar velocity fields (W1, H1 and W2). A configuration with a black hole set on a circular orbit did not produce significantly different results compared to similar configurations with the same mass and amplitude u_o (case W1c, Table 3). Taken together, these results highlight the importance of the black hole effective orbital cross section $\propto u_o^2$ in transferring binding energy to the stars.

5 Discussion

Oscillations of a massive black hole about the centre of a host galaxy leave a signature on the kinematics of surrounding stars. We showed from an analytic harmonic potential model that stars on circular orbits lose or gain energy according to the relative phase between their and the black hole's orbit: for an evenly sampled distribution function, half of the stars gain energy, the other half loses energy. The black hole plays the role of a catalyst by allowing energy exchanges between the stars.

We explored a range of orbits with black hole and stars in a logarithmic potential with an Bulirsch-Stoer numerical integration scheme (Press et al. 1992) using on the order of 10^5 orbits. The feedback of stars on the black hole orbit was neglected, an approach motivated by the large black hole to stellar mass ratio. With stars set on circular orbits, we found a strong response to black hole motion, at distances
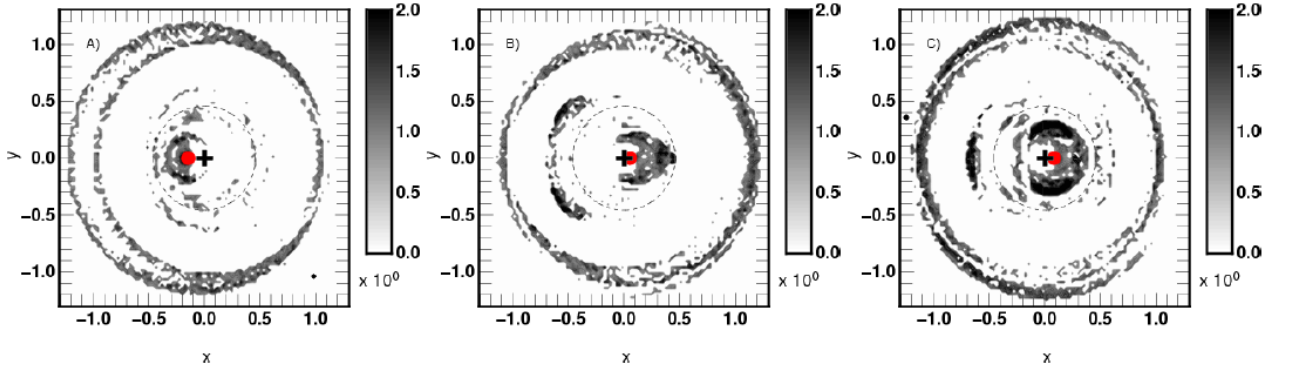
Figure 14. Maps of the Toomre number Q_J for the reference calculation C3 at A) t = 15; B) t = 16 and C) t = 17 time units of evolution. The shade indicates stability to fragmentation modes. The white regions have $Q_J < 1$ and would be susceptible to fragment.

ranging up to 3 or 4 times the black hole's radius of influence (see Fig. 5 and 9). Such a strong response was also seen in perturbed circular orbits, with velocity perturbations in the range ±10%. We quantified the impact of black hole motion on the stars' energy distribution function. We measured root-mean square deviations growing linearly with the amplitude of motion, $u_o = R_o/R_c$, where R_c is the core-radius of the logarithmic potentials. We obtained a significant response (signal-to-noise ratio > 4) even for modest amplitudes of $\sim r_{bh}/3$, where r_{bh} is the black hole's radius of influence (cf. Eq. 5 and Table 3). Worried that these results concerned circular or near-circular orbits only, we reset the velocity field ('warm' and 'hot' configurations, see §4) but kept the original energy distribution function unchanged. This resulted in washed out features in maps of the surface density and velocity dispersion (see Fig. 12) but left a signature on the energy d.f. of the same magnitude, with once again the black hole amplitude of motion the main agent responsible for re-shaping the energy d.f. (Table 3). An analysis of the angular momentum d.f. showed that non-circular orbits visit the centre more frequently and couple more strongly with the black hole at some point on their orbit. Thus, although the energy exchange mechanism identified for circular orbits plays a secondary role in systems with warm and hot velocity fields, the black hole motion still induced strong anisotropy. This was most clearly seen when profiling the net line-of-sight velocity v_{1d} resulting from two different projection angles (see Fig. 12, right-hand panels). Any level of anisotropy is attributable to the motion of the black hole, since a static hole would have left the initial isotropic d.f. unchanged.

5.1 Comparison with MW data

The largest values of v_{1d} were obtained from a viewing angle parallel to the motion of the black hole. Contrasting these values to the root mean square velocity dispersion, we find a ratio of $< |v_{1d}| > / \sqrt{<v_{1d}^2>} \approx 25\%$ at maximum value, inside the hole's radius of influence (see Fig. 11 and 12). Applying this to Milky Way data, where the mean velocity dispersion rises to ~ 180 km/s inside 1 pc of Sgr A$\star$ (Genzel et al.1996) we obtain streaming velocities in the range ~ 40

km/s, a rough match to the values reported recently by Reid et al. (2006). The surface density profile shows a break at radius $r_{br} \sim 0.2$ pc (Schödel et al. 2007). Inside r_{br}, the volume density is fitted with a power-law index $\gamma \simeq 1.2$ which falls outside the range 3/2 to 7/4 of the Bahcall-Wolf solution. Black hole motion of an amplitude $R_o \sim r_{br}$ might cause such a break. The ratio $r_{br}/r_{bh} \sim 0.2$ compares well with the value ≈ 0.3 adopted for our reference calculation (Table 1).

5.2 Circular black hole orbit

We worried that a black hole set on a radial orbit might trigger only a subset of resonant modes from the stars, in contrast to the more probable situation where the hole's orbit has a finite angular momentum. Recall the analysis of §2.2, where the response was stronger for aligned orbital angular momenta. To test this idea, we re-ran the 'warm' W1 calculation with the black hole now set on a circular path at a radius $u_o = R_o/R_c = 0.097$, or $\simeq 50\%$ its radius of influence (cf. W1c, Table 1 and 3). As the black hole orbits the centre, an $m = 0$ density mode develops which shows up as a trailing arm on Fig. 12, bottom row, middle panel. The black hole orbit is anti-clockwise. The arm stretches radially from 1 to ≈ 2 times r_{bh}. Its integrated mass $\simeq 40\%$ the black hole's mass, and so if the gravity of the arm were taken into account, the torque that this would produce would modify the black hole's orbit significantly, an effect which was neglected here. The averaged line-of-sight velocity of the stars, on the other hand, showed spatial variations of the same amplitude as in the other cases with a strictly radial black hole orbit of a similar amplitude. This result comforts the thought that black hole motion may yet give rise to an observable kinematic signature (especially in the profile of v_{1d}), regardless of the precise parameters of its orbit.

5.3 Jeans instability

Our approach suffers from a severe limitation, in that it does not integrate the full response of the stars to their own density enhancements. These could become bound structures

which would alter the dynamics globally. To inspect whether this could have an influence over the evolution of the velocity field, we computed the Toomre number

$$Q_J \equiv \frac{\sigma\Omega}{G\Sigma} = \frac{\sigma^2}{G\Sigma \mathrm{d}l}$$

at each mesh points of the simulations space. Here the mesh size $\mathrm{d}l \simeq 0.02$, and the velocity dispersion σ given by (31) is measured with respect to the initial circular flow. The surface density Σ is calculated as before with an CIC algorithm. Stars are stable against self-gravitating local modes of fragmentation when $Q_J \gtrsim 1.7$ (see e.g. Binney & Tremaine 1987). We applied a modified criterion for stability, because the disc is presumed stable against such modes initially, that is, when the black hole is fixed at the centre of coordinates and the system is axially symmetric. We subtracted from the local mean square velocity dispersion the value computed for the symmetric configuration. In this way we measure only the increase in dispersion due to black hole motion, and set a conservative threshold for stability such that $Q_J > 1$. When that condition is satisfied, the black hole contributes more than 58% of the square velocity dispersion required to prevent local self-gravitating fragmentation modes from growing through its orbital motion alone. Since the black hole already contributes more than 50% to the gravity everywhere inside its radius of influence, it also provides the extra dispersion required to kill off all self-gravitating modes.

Fig. 14 maps out Q_J at three different times for the reference calculation C3; the shaded area is for $Q_J > 1$ with an upper cutoff at 2, so white means instability on that figure. These images should be compared to their counterpart on Fig. 9. It is notable that most of the over-dense thin structures on that figure appear *un*stable against fragmentation on Fig. 14 (since they disappear in a sea of white). The outer dark ring at $r \simeq 1.3$ on the figure matches the position of the 2:5 resonance shown on Fig. 8 (using $R_c \simeq 0.46$ to revert to physical dimensions). Thus it is very likely that structures that would cross this area would be heated up and disrupted as a result of black hole motion. This may have consequences for the streams of stars observed at the centre of the MW (Genzel et al. 2003). The dimensions of this ring, of some $3r_{bh}$, would correspond to a radius of (roughly) 3 pc for the MW. This should be an element to incorporate into future modelling of the MW centre since actual resolution power already resolves sub-parsec scales.

6 Conclusions and future work

The response of stellar orbits is in direct proportion to the amplitude of motion of a massive black hole. The imprint of black hole motion on the stellar kinematics is in direct relation to the stars' angular momentum distribution function. Stars on low-angular momentum orbit likely will collide with the hole, while those of large momenta experience strong beat-frequency resonances (when the hole's orbit is either radial or circular). The combined effect left the velocity field significantly anisotropic with a ratio of averaged one-dimensional velocity to rms dispersion reaching $\sim 18\%$. Because analysis suggests that the black hole energy is preserved while that of the stars varies in time, we say the the

black hole is a catalyst for evolution of the stellar energy d.f..

The two-dimensional modelling done in this paper is a first attempt at isolating the generic features of a time-evolving dense nuclei with black hole motion. The quantitative outcome of the calculations would be improved in a study of a family of anisotropic distribution functions, such as e.g. the Osipkov-Merritt d.f. $f(E - L^2/r_a^2)$ (Binney & Tremaine 1987, §4.4.4), using self-consistent three-dimensional integrators. We have shown that when stars are on circular or near-circular orbits, the resonances induced by the black hole likely will lead to self-gravitating substructures inside a volume of a few times r_{bh} in diameter. Such a study carried out with an N-body technique is possible provided that collisional physics around the black hole is well resolved (Preto et al. 2004). Merritt (2005) and Merritt et al. (2007) have shown that repeated collisions with stars inside $\sim r_{bh}/2$ lead to random walk and an effective 'Brownian' velocity transferred to the black hole. If the random walk was of amplitude $r_{bh}/2$, this would equally imprint the kinetic motion of stars outside $\sim r_{bh}$, as we have seen, through the catalytic process that we have outline.

We have neglected the orbital evolution of the black hole. In reality the stars inside the black hole's radius of influence r_{bh} would take away energy and lead to it sinking to the centre through dynamical friction. This does not invalidate the impact of black hole motion on the stellar kinematics because 1) this signature is manifest well outside $\sim 2r_{bh}$ and 2) dynamical friction will be effective on a time-scale of $\sim$ few orbital revolutions. Recall that the effect discussed here is effective on a single black hole period.

Black hole orbital evolution would bring a higher degree of realism and a more fiducial comparison to observational data. We examined the case of a black hole on a circular orbit which gave rise to an $m = 0$ density wave, spanning a mass of $\sim 40\%$ the mass of the black hole. The gravitational torque of the wave would rapidly brake the black hole, which would sink toward the centre and lock many stars along with it. If the wave were unstable to collapsing on itself and form a bound object, a double nucleus would form. The separation between the two nuclei would be $\sim 2r_{bh}$ or larger, as deduced from the density map on Fig. 12, panels at the bottom. On the contrary, if the tidal field of the BH were too strong, the wave would merge with the black hole. This would leave the black hole near the galactic centre surrounded by a pool of stars on eccentric orbits. Tremaine (1995) has argued that the double nucleus of M31 (Lauer et al. 1993) may be such a case of an off-centre supermassive BH surrounded by a stretched Keplerian disc of size $\sim r_{bh}/2$ (0.5" separation at 800 pc, with $M_{bh} \simeq 8 \times 10^7 M_\odot$). Our calculations did not include self-gravity, and hence the fate of the $m = 0$ density wave seen on Fig. 12 remains undetermined. (See also Peiris & Tremaine 2003, Salow & Statler 2001, and Bender et al. 2005 for further data on M31.) Other double or multiple nuclei detected in external galaxies (e.g., NGC4486B and NGC4382, Lauer et al. 1996, 2005; the Virgo Cluster dwarf VCC 128, Debattista et al. 2006) are prime examples of the strong orbital coupling of stars with a supermassive black hole and its influence on the small-scale morphology of a galaxy. New data may reveal cases where double-nuclei galaxies result from the orbital coupling we have discussed here. For the Milky Way, current and future high-precision

astrometric missions, such as RAVE (accuracy of ~ 1 km/s out to 8 kpc at a magnitude limit of ~ 13 [*I*-Band]) or GAIA (launch date 2011) should pick up any systematic trends in stellar kinematics and set firm constraints on any black hole motion inferred from stellar streams.

ACKNOWLEDGMENTS

REFERENCES

Backer, D.C. & Sramek, R.A. 1999, ApJ 524, 805
Bahcall, J.N. & Wolf, R.A 1977, ApJ 216, 883
Begelman, M.C., Blacndford, R.D. & Rees, M.J. 1984, RvMP 56, 255
Binney, J.J. & Tremaine, S.D. 1987, Galactic Dynamics, Princeton: University Press
Debattista, V. P., et al. 2006, ApJ 651, L97
Freitag, M., Amaro-Seoane, P. & Kalogera, V. 2006, ApJ 649, 91
Genzel, R., Thatte, N., Krabbe, A., et al. 1996, ApJ 472, 153
Genzel, R., Eckart, A., Ott, T., et al. 1997, MNRAS 291, 219
Genzel, R., Schdel, R., Ott, T., et al. 2003, ApJ 594, 812
Ghez, A. M., Salim, S., Hornstein, S. D., et al. 2005, ApJ 620, 744
Kormendy, J. & Richstone, D. 1995, ARA&A 33, 581
Lauer, T. R., Faber, S. M., Groth, E. J., et al. 1993, AJ 106,1436
Lauer, T. R., Tremaine, S., Ajhar, E.A., et al. 1996, ApJ 471, L79
Lauer, T.R., Faber, S.M., Gerbhardt, K., et al. 2005, AJ 129, 2138
Lynden-Bell, D. 1979, MNRAS 187, 101
Merritt, D. 2001, ApJ 556, 245
Merritt, D. 2005, ApJ 628, 673
Merritt, D. 2006, RPPh 69, 2513
Merritt, D., Berczik, P. & Laun, F. 2007, AJ 133, 553
O'Leary, R.M. & Loeb, A. 2006, submitted to MNRAS, astro-ph/0609046
Peiris, H.V. & Tremaine, S.D. 2003, ApJ 599, 237
Press, W.H. et al. 1992, Numerical Recipes in Fortran, 2nd Ed., (Cambridge: Cambridge University Press)
Preto, M., Merritt, D. & Spurzem, R. 2004, ApJ 613, L109
Rauch, K.P. & Tremaine, S.1996, NewA 1, 149
Reid, M. J., Menten, K. M., Trippe, S., et al. 2006, submitted to ApJ, astro-ph/0612164
Salow, R. M. & Statler, T. S. 2001, ApJ 551, L49
Schödel, R., Eckart, A., Alexander, T., et al. 2007, astro-ph/0703178
Toomre, A. & Toomre, J. 1972, ApJ 178, 623
Tremaine, S. D. 1995, AJ 110, 628
Yu, Q. & Tremaine, S.D. 2003, ApJ 599, 1129
Zhao, H, Haennelt, M.G. & Rees, M.J. 2002, NewA 7, 385